Geochemistry Geophysics Geosystems G3

Article
Volume 13, Number 6
9 June 2012
Q06007, doi:10.1029/2012GC004119
ISSN: 1525-2027

Published by AGU and the Geochemical Society

High-resolution body wave tomography models of the upper mantle beneath eastern China and the adjacent areas

Liang Zhao
State Key Laboratory of Lithospheric Evolution, Institute of Geology and Geophysics, Chinese Academy of Sciences, 19 Beituchengxi Road, P.O. Box 9825, Beijing 100029, China (zhaoliang@mail.igcas.ac.cn)

Richard M. Allen
Seismological Laboratory, University of California, Berkeley, California 94720, USA (rallen@berkeley.edu)

Tianyu Zheng and Rixiang Zhu
State Key Laboratory of Lithospheric Evolution, Institute of Geology and Geophysics, Chinese Academy of Sciences, 19 Beituchengxi Road, P.O. Box 9825, Beijing 100029, China (tyzheng@mail.igcas.ac.cn; rxzhu@mail.igcas.ac.cn)

[1] We present new 3-D tomographic models of V_P, V_S and V_P/V_S ratio anomalies in the upper mantle beneath EC and adjacent areas. This data was collected and interpreted with the goal of clarifying geodynamic processes that caused spatially variable event histories throughout Eastern China (EC) during Mesozoic to Cenozoic time. The tomographic images were constructed by inverting body wave travel-times recorded at ~1300 stations within the upgraded China National Seismic Network, and 9 temporary arrays. Resolution tests for different depths and the featured velocity anomalies verify that the tomographic images capture the velocity heterogeneities in the upper mantle to depths of 700 km. The salient features of V_P, V_S and V_P/V_S ratio anomalies can be clearly identified. These include strong multiscale heterogeneities occupying the upper mantle beneath EC and differences in the spatial scale of anomalies found beneath northern and southern areas of EC. These features demonstrate a degree of spatial variability in the geodynamic evolution of EC. We propose two mechanisms to explain these patterns. First, the western front of the subducted slab may have imparted greater horizontal compressional stress in areas where it impinged further eastward into EC. These areas would experience stronger convection and an altered stress regime in the upper mantle, creating significant thermal anomalies beneath the South China Block (SCB) relative to the eastern North China Craton (NCC). Second, differing thermal states and viscosities for the eastern NCC and the Cathaysia Block (CaB) resulted in differing responses to regional deformation. The Archean hinterland of the eastern NCC specifically has a colder thermal state and higher viscosity, and therefore exhibits only small-scale heterogeneities due to the effect of shear localization. The Neoproterozoic CaB has a relatively warm thermal state with lower viscosity, and thus deformed more continuously.

Components: 8500 words, 13 figures.

Keywords: body-wave tomography; eastern China; upper mantle structures.

Index Terms: 7208 Seismology: Mantle (1212, 1213, 8124); 7270 Seismology: Tomography (6982, 8180); 8170 Tectonophysics: Subduction zone processes (1031, 3060, 3613, 8413).

Received 23 February 2012; **Revised** 4 May 2012; **Accepted** 5 May 2012; **Published** 9 June 2012.

Zhao, L., R. M. Allen, T. Zheng, and R. Zhu (2012), High-resolution body wave tomography models of the upper mantle beneath eastern China and the adjacent areas, *Geochem. Geophys. Geosyst.*, *13*, Q06007, doi:10.1029/2012GC004119.

1. Introduction

[2] As the eastern margin of the Eurasian plate, Eastern China (EC) records the geodynamic evolution associated with the ongoing convergence of Eurasia and the Paleo- Pacific and Philippine plates initiated during Mesozoic to Cenozoic time (Figure 1). Previous multidisciplinary studies have shown that the deformation of EC associated with plate convergence exhibits significant temporal and spatial variability that generally conforms to north, south, east and west boundaries of the region's major tectonic provinces [e.g., *Ren et al.*, 2002; *Wu et al.*, 2005; *Niu*, 2005; *Wang et al.*, 2006; *Li and Li*, 2007; *Sun et al.*, 2007; *Yang et al.*, 2008; *Yin*, 2010; *Zheng et al.*, 2012]. EC therefore provides an excellent natural laboratory for studying continental margin deformation in response to subduction. The geodynamic processes responsible for temporal and spatial patterns of deformation in this region have been examined and discussed at length, but without consensus on a consistent interpretation of the observations.

[3] Detailed information on subsurface velocity structure can provide an important perspective on the geodynamic evolution of areas affected by protracted episodes of subduction. Within the last two decades, tomographic experiments have elucidated the mantle structure beneath different regions of China [e.g., *Lebedev and Nolet*, 2003; *Hearn et al.*, 2004; *Zhao et al.*, 2004; *Lei and Zhao*, 2005; *Huang and Zhao*, 2006; *Li et al.*, 2006, 2008; *Sun and Toksöz*, 2006; *Chang et al.*, 2007; *Sun et al.*, 2008a, 2008b; *Tian et al.*, 2009; *Xu and Zhao*, 2009; *Zhao et al.*, 2009; *Li and van der Hilst*, 2010; *Feng et al.*, 2010; *Obrebski et al.*, 2012]. Previous tomographic studies of the EC have been based on either V_P or V_S parameters derived from different data sources, making it difficult to establish consistent V_P/V_S models. Previous tomographic studies in China have also been constrained by limited seismic station coverage, and thus reported only on localized or continental scale features. High-resolution tomographic images and more detailed information on upper mantle structure can provide a better picture of deformation and the overall geodynamic evolution of EC.

[4] This study capitalized on recent upgrades in the China National Seismic Network (CNSN), which provides adequate to relatively dense station coverage throughout EC. Data was also collected using portable stations across key tectonic units and boundaries. The combined V_P, V_S and V_P/V_S ratio models described here are based on enhanced station coverage and thus provide novel, high-resolution information on the region's geodynamic response to subduction.

2. Geological Background

[5] We use the term "Eastern China" to describe the Chinese part of the eastern margin of the Eurasian plate that is tectonically linked to the subduction of the Pacific and Philippine Sea plates (Figure 1). For the sake of this study, EC is divided into three blocks from north to south: the Northeastern China Block, the North China Craton (NCC) and the South China Block (SCB). Along EC's eastern margin, the Pacific and Philippine Sea plate subduction zones extend beneath the Eurasian plate. The NE trending Xing'an-Mongolian orogenic belt welds the northern part of EC to the Siberian Craton. To the southwest, the NW-SE trending Longmenshan fault separates EC from the Tibetan Plateau.

2.1. Tectonic Origins of EC

[6] EC consists of a series of Phanerozoic orogenic belts welded together by Late Paleozoic to Early Mesozoic tectonic events. Prior to its amalgamation, EC could be divided into two separate tectonic provinces - the NCC and the SCB, both of which exhibit unique inherited properties. The NCC preserves continental rocks as old as 3.8 Ga [*Liu et al.*, 1992]. *Zhao et al.* [2001] proposed that the NCC formed during Paleoproterozoic amalgamation of eastern and western Archean blocks. Basement units of the NCC are overlain by thick sedimentary sequences of Meso- to Neoproterozoic and Paleozoic age. The relative scarcity of Paleozoic igneous units implies that the NCC was tectonically stable throughout the early Phanerozoic [*Wu et al.*, 2003]. From the Late Permian to Early Triassic, the NCC collided with accreted terranes of the Central Asian Orogenic Belt (CAOB). This last formational episode occurred after the Paleo-Pacific oceanic lithosphere had begun subducting beneath the northern margin of the NCC [*Xiao et al.*, 2003].

[7] The SCB consists of the Archean Yangtze Craton (YC) to the northwest and the Cathaysia

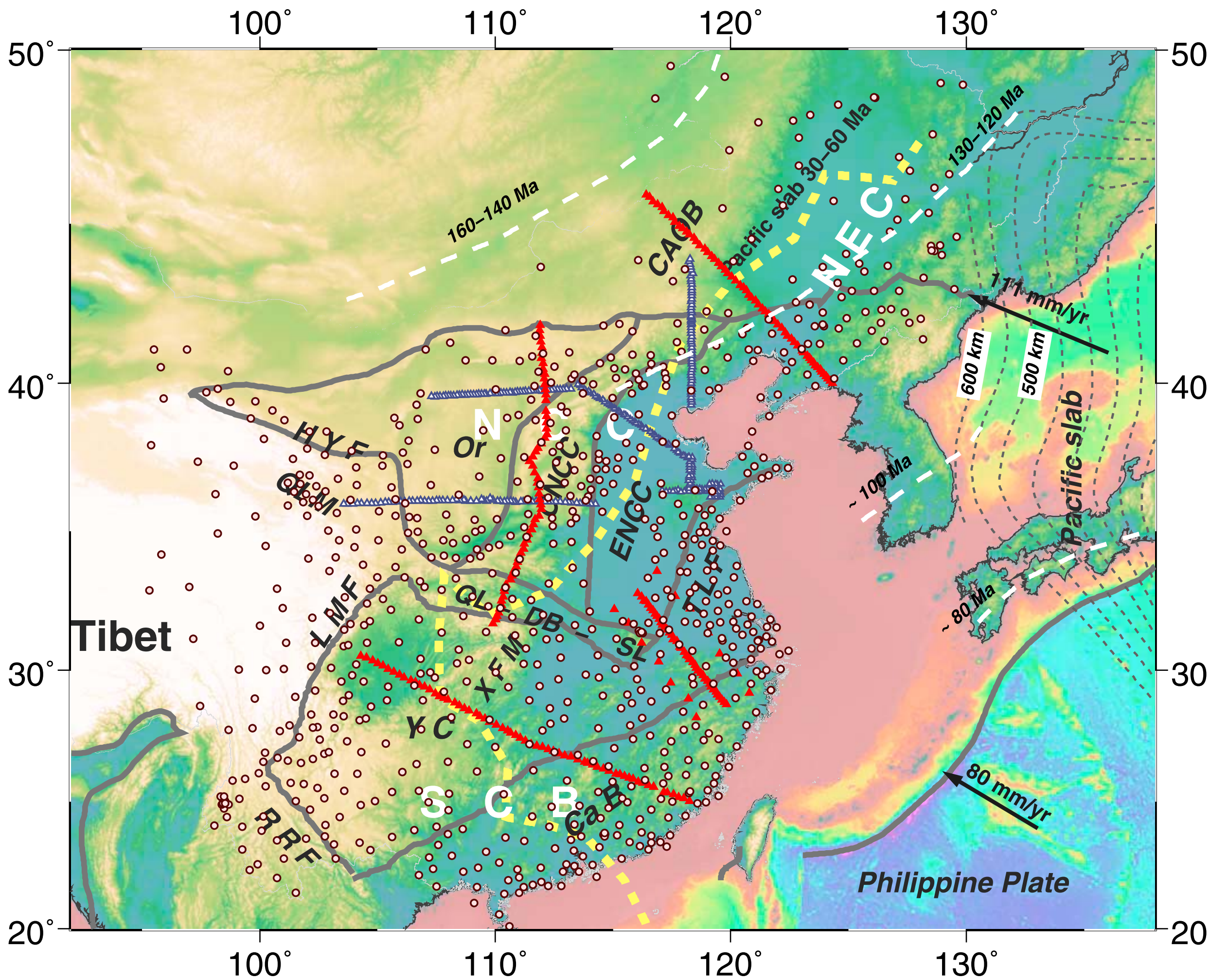

Figure 1. Regional map showing major tectonic features and seismic station locations used to construct tomographic images. The open circles mark permanent stations of the China National Seismic Network (CNSN). The triangles mark portable stations from a network operated by the Institute of Geology and Geophysics, Chinese Academy of Sciences (IGGCAS): blue triangles mark stations used in a previous study [*Zhao et al.*, 2009]; red triangles mark stations used in this study. Grey lines demarcate the major tectonic provinces in Eastern China (EC) and adjacent areas. Black arrows represent the absolute plate motion [*Gripp and Gordon*, 2002]. The dotted lines show the depth contours of the Wadati-Benioff deep seismic zone [*Lei and Zhao*, 2005]. The yellow dashed line marks the slab front of the Pacific plate from 30 to 60 Ma [*Wen and Anderson*, 1995]. The white dashed lines show the spatial and temporal trends of peak magmatism in NE Asia [*Wang et al.*, 2006]. NEC: Northeastern China; CAOB: Central Asian Orogenic Belt; NCC: North China Craton; Or: Ordos Block; CNCC: central part of the NCC; ENCC: eastern NCC; SCB: South China Block; YC: Yangtze Craton; CaB: Cathaysia Block; QLM: Qilian orogenic belt; TLF: Tanlu Fault zone; QL-DB-SL: Qinling-Dabie-Sulu orogenic belt; LMF: Longmenshan Fault; XFM: Xuefeng Mountain; HYF: Haiyuan Fault; RRF: Red River Fault.

Block (CaB) to the southeast (Figure 1). The oldest igneous rocks found within the YC give a weighted mean U-Pb age of ~3.2 Ga [*Jiao et al.*, 2009] while zircons from the oldest known metamorphosed basic-ultrabasic rocks within the CaB give U-Pb ages of ~1.85 Ga [*Xiang et al.*, 2008]. Consensus holds that the YC and CaB were conjoined by the late Neoproterozoic. A protracted period of widespread magmatism implies that the CaB underwent multiple episodes of reactivation during the Phanerozoic. Recent in situ Hf and O isotope analyses of detrital zircons from CaB units indicate periods of crustal growth at ca. 1870 Ma, ca. 1400 Ma, ca. 1140–940 Ma, ca. 445 Ma and ca. 280 Ma, alternating with crustal recycling at ca. 1200 Ma, ca. 830 Ma and ca. 370 Ma [*Li et al.*, 2012]. Given the multiphase history of the CaB, researchers have not been able to identify the exact boundary between the YC and the CaB.

[8] The formation of EC was completed by Late Jurassic time with the amalgamation of the NCC and the SCB [*Zhang*, 1997; *Faure et al.*, 2001; *Meng and Zhang*, 2000]. Paleomagnetic data and sedimentary records indicate that convergence occurred from the Late Permian to Middle Jurassic time and resulted in a ~70° clockwise rotation of the SCB with respect to the NCC [*Zhao and Coe*, 1987; *Meng et al.*, 2005]. This collision produced the E-W-trending Qinling-Dabie-Sulu ultrahigh-pressure orogenic belt.

2.2. Tectonism Related to Pacific Plate Subduction

[9] EC became an active continental margin prior to the Jurassic period [*Zhou and Li*, 2000; *Wang et al.*, 2006; *Li and Li*, 2007] due to the initiation of subduction of the Paleo-Pacific plate. Geological and geochemical evidence indicates that EC underwent multiple episodes of deformation that included high heat-flow [*Hu et al.*, 2000], widespread tectonic extension [e.g., *Ren et al.*, 2002] and numerous magmatic events from Late Mesozoic to Cenozoic time [e.g., *Wu et al.*, 2005, 2011; *Wang et al.*, 2006; *Li and Li*, 2007]. The subduction related deformation of EC shows distinct spatiotemporal variations. The Northeastern China Block and the NCC include wide, uninterrupted basins and multiphase magmatic events whereas the SCB includes Basin and Range-like extensional features and a relatively continuous magmatic history. The three blocks can be differentiated according to their distinct spatiotemporal units described below.

[10] (1) The Northeastern China Block includes a Paleozoic orogenic collage that comprises the eastern flank of the Central Asian Orogenic Belt. Mesozoic magmatic events show eastward migration trends from southeastern Mongolia to southwestern Japan [*Wang et al.*, 2006]. Recent geochronologic data collected from Phanerozoic granitoids suggest that Northeastern China was significantly affected by subduction of the Paleo-Pacific plate during Mesozoic to Cenozoic time [*Wu et al.*, 2011].

[11] (2) In contrast to the long-term stability of the Ordos Block, parts of eastern NCC have experienced significant lithospheric thinning. This province was originally composed of relatively thick (~200 km) Archean or Proterozoic lithosphere that was significantly attenuated to ~80 km thickness during Late Mesozoic to Cenozoic time [e.g., *Griffin et al.*, 1998; *Chen et al.*, 2008; *Zheng et al.*, 2008; *Zhu and Zheng*, 2009]. Lithospheric thinning coincided with the development of a series of wide, uninterrupted basins [*Ren et al.*, 2002]. Recent receiver function imaging, tomography and shear wave splitting studies [*Chen et al.*, 2008; *Zhao et al.*, 2009; *Zhao and Xue*, 2010; *Zhao et al.*, 2011] suggest that lithospheric reactivation extended beneath the central NCC during the Cenozoic.

[12] (3) In contrast to the relatively stable YC, the CaB has experienced extensive tectonism [e.g., *Li*, 2000; *Wang et al.*, 2005]. The CaB includes a Basin and Range–like extensional province that contrasts wider basins (widths >600 km) found in the eastern NCC. Magmatic activity affected a ~1000 km area from the continental margin to the southeast edge of the YC [*Li and Li*, 2007] and temporally coincided with extensional deformation of the CaB. Geochemical analyses of 280 Ma detrital zircons from YC units reveal significant negative correlations between ϵHf(T) and δ^{18}O values, indicating that YC igneous units formed from reworked, ancient supracrustal materials and mantle-derived magmas in an active continental margin setting [*Li et al.*, 2012]. Equilibrium temperatures estimated by two-pyroxene geothermometry vary from 994°C to 1081°C, indicating that the Mesozoic lithospheric mantle had a relatively steep geothermal gradient [*Liu et al.*, 2012].

3. Data and Method

3.1. Data Processing

[13] This study uses seismic events collected from two separate data sets. The first data set was collected from 738 permanent stations of the CNSN evenly distributed throughout the study area (circles in Figure 1), operating from July 2007 to May 2010 [*Zheng et al.*, 2010]. In order to enhance the resolution beneath the key tectonic boundaries, a second data set was drawn from all available temporary seismic networks deployed by the Institute of Geology and Geophysics, Chinese Academy of Sciences (IGGCAS). The IGGCAS networks consist of 4 temporary linear sub-arrays (red triangles in Figure 1), which operated sequentially from December 2007 to May 2010. Most stations were equipped with Güralp CMG-3ESP or 3T sensors (50 Hz to 30, 60 or 120 s) and REFTEK-72A or 130 data loggers. Each array was deployed for 12–18 months.

[14] Events with epicentral distances ≥30° from the study area were selected (Figure 2) for tomographic processing. Relative travel times of direct P- and S-waves were calculated with respect to theoretical

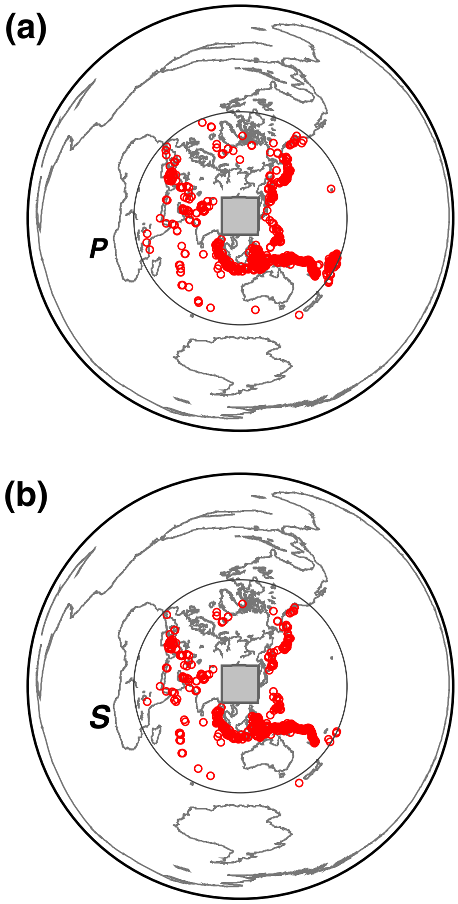

Figure 2. Location of events (red circles) used for (a) P wave and (b) S-wave inversion. Gray rectangle represents the study area.

travel times using IASP91 model assumptions [*Kennett and Engdahl*, 1991]. A multichannel cross-correlation technique [*Vandecar and Crosson*, 1990] was used to measure differential travel times in four frequency bands: 0.02–0.1 Hz, 0.1–0.8 Hz, 0.4–0.8 Hz and 0.8–2.0 Hz. Figures S1 and S2 in the auxiliary material present examples of travel-time measurements for vertical and transverse components, respectively.[1] To reduce the influence of unevenly distributed events on the inversion step, events with higher signal-to-noise ratio were selectively processed. To enhance the regional sampling coverage within the NCC, we also selected ~18,000 P wave and ~10,000 S-wave arrival events from 5 other IGGCAS sub-arrays (blue triangles in Figure 1) used by *Zhao et al.* [2009]. In combining the data, we found that all four frequency bands have good signal-to noise ratios for P wave arrivals. The 0.4–0.8 Hz band however provided the best signal-to-noise ratio and contributed up to 59,512 relative travel-time residuals for our inversion. A total of 37,569 S-wave arrivals were selected from the 0.02–0.1 Hz band. Other frequency bands were dominated by noise. The average cross-correlation coefficient is 0.95 for both P- and S-waves. The average standard deviations in delay times from cross-correlation calculations are 0.003 s for P waves and 0.01 s for S-waves. Figure 3 shows pairs of P- and S-wave relative travel-time residuals for common stations and events.

[1]Auxiliary materials are available in the HTML. doi:10.1029/2012GC004119.

3.2. Crustal Correction

[15] Introduction of crustal models provides tomographic imaging procedures with a more reliable velocity distribution for the upper mantle [e.g., *Ekström and Dziewonski* 1998; *Allen et al.*, 2002; *Li et al.*, 2006; *Koulakov et al.*, 2009]. To avoid intermingling of crustal and upper mantle signals, we employ crustal velocity and thickness models to calculate theoretical ray travel-time corrections for heterogeneity within the crust. Previous studies of the EC have developed V_S crustal models based on Rayleigh wave dispersion [*Huang et al.*, 2003, 2009] and based on local body wave tomographic imaging [*Sun et al.*, 2008a]. Sensitivity tests of each of these crustal models indicated no significant difference between mantle model results. We therefore only present the tomographic model

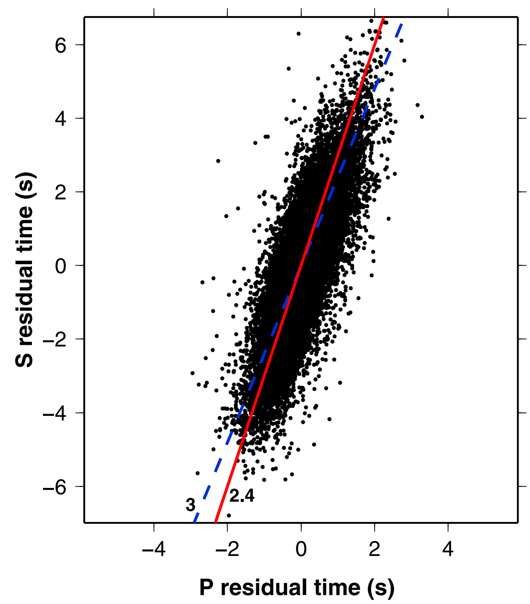

Figure 3. Pairs of P- and S-wave relative travel-time residuals for common stations and events. The dashed blue line and red line indicate reference trends with their slope values labeled at bottom.

generated using *Sun et al.*'s [2008a] crustal model based on body wave tomography.

[16] Receiver function studies [*Ai et al.*, 2007; *Wei et al.*, 2011] demonstrate that the crustal V_P/V_S ratio varies from 1.70 to 1.84 with a mean value of 1.76 in the SCB and a mean value of 1.77 in the NCC. The mean crustal V_P/V_S ratio of 1.765 was used a priori to calculate correction times for P wave arrivals. To estimate the influence of V_S to V_P scaling, we calculated relative error for the time correction using different V_P/V_S ratios. Comparison of errors with those calculated using a mean V_P/V_S value showed that the relative error is negligible. The P wave tomographic inversions described in the following section also demonstrate that variation in the V_P/V_S ratio (between 1.70 and 1.84 in practice) has only a small influence on the final images generated.

3.3. Methods

[17] The tomographic model space is a ~3300 km by 3300 km area (in the east-west and north-south directions, respectively) that extends to 2500 km depth, centered at 112°E, 35°N. The image volume was parameterized within a grid-space defined by regular nodes at 52 km by 52 km by 39 km. The P- and S-wave data sets were used to construct matrices based on both theoretical ray [e.g., *Allen et al.*, 2002] and finite-frequency kernel formulations [*Dahlen et al.*, 2000; *Hung et al.*, 2000]. The damped LSQR algorithm [*Paige and Saunders*, 1982] was then used to invert the matrix. The damping parameters were empirically determined based on the trade-off between model norm and variance reduction of data. The models discussed in this paper were constructed using damping parameters that yield a variance reduction of ~83% for both V_P and V_S. Figure S3 in the auxiliary material illustrates the tradeoff between model norm and variance reduction for the V_P and V_S models based on finite frequency kernel method. To account for any baseline shift between the relative travel-time sets for different events, event corrections were included in the inversion [*Allen et al.*, 2002].

4. V_P, V_S and V_P/V_S Ratio Models

[18] Tomographic results of V_P, V_s and V_P/V_s ratio anomalies are shown in Figures 4 to 6 in both horizontal map views and cross-sectional depth slices. Our results show that structures imaged using finite frequency sensitivity kernels (Figure 4) and ray-based methods are very similar except that the kernel-based models yield higher root-mean square amplitudes for P- and S-wave velocity perturbation, as expected [e.g., *Hung et al.*, 2004]. For convenience, we hereafter focus our discussion on the kernel-based results.

[19] The new P- and S-wave models are broadly consistent despite differences in the wavelengths of phases used and in station density. The V_P/V_S ratio model negatively correlates to the P- and S-wave models but shows more small-scale variation. P- and S-wave models also show spatial patterns consistent with those identified in previous studies [e.g., *Huang and Zhao*, 2006; *Li et al.*, 2006, 2008; *Sun et al.*, 2008a, 2008b; *Tian et al.*, 2009; *Zhao et al.*, 2009; *Li and van der Hilst*, 2010; *Feng et al.*, 2010]. Our procedures however provide greater resolution and permit detection of certain features in more detail. Resolution tests given in section 5 demonstrate that the tomographic images provide reliable depictions of velocity heterogeneities in the upper mantle to depths of 700 km.

[20] An overview of the results (Figures 4 to 6) reveals strong multiscale heterogeneities (H1, H2, L1, L2, L3 in Figure 5) extending from the uppermost mantle to the mantle transition zone beneath EC. Given better data coverage for the NCC and the SCB, we focus on the structures beneath these two regions, and not Northeastern China. The V_P, V_S and V_P/V_S images consistently display a pronounced contrast in the wavelength of the velocity anomalies occurring beneath the NCC and the SCB. In the NCC, complex, small-scale low-velocity structures are widespread in central and eastern areas. In the SCB, the YC subsurface is high velocity while the CaB subsurface is predominantly low velocity.

4.1. The North China Craton (NCC)

[21] The strong contrast in the between the Ordos Craton and the eastern NCC is an obvious feature of NCC tomographic images (Figures 4a, 4b, 4e, 4f, 5a, 5b, 5e, and 5f). A high-velocity region extends to >330 km depth beneath the Ordos craton (Or, H1 in Figure 5). A narrow, north-south trending, low-velocity region (with dimension of ~800 km north-south by 200–300 km east-west) is located at the base of the central NCC lithosphere (L1 in Figure 5) [*Zhao et al.*, 2009]. This region broadens to include much of the area beneath eastern NCC in deeper zones of the upper mantle. Cross-sectional depth slices of this low-velocity anomaly (L1; Figures 5a, 5b, 5e, and 5f) clearly illustrate that it extends from 100 km depth to the mantle transition zone beneath the central and eastern NCC. These findings are consistent with receiver function studies that imaged a similarly

10.1029/2012GC004119

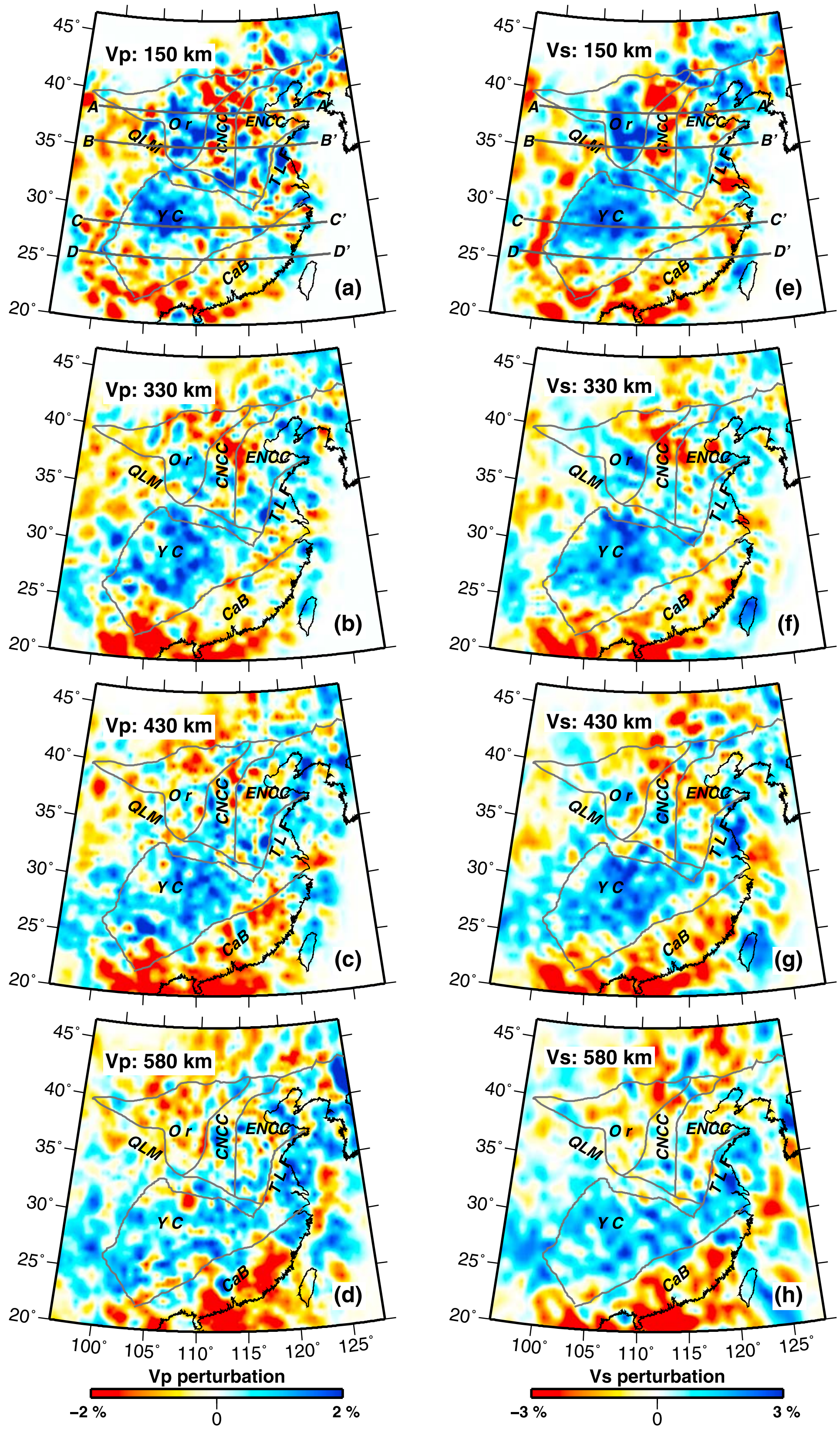

Figure 4. Upper mantle depth slices from the V_P and V_S models resolved from finite-frequency tomography. (a–d) P wave velocity perturbations at different depths and (e–h) S-wave velocity perturbations at different depths. Lines A-A′, B-B′, C-C′ and D-D′ represent the location of cross-sections shown in Figure 5.

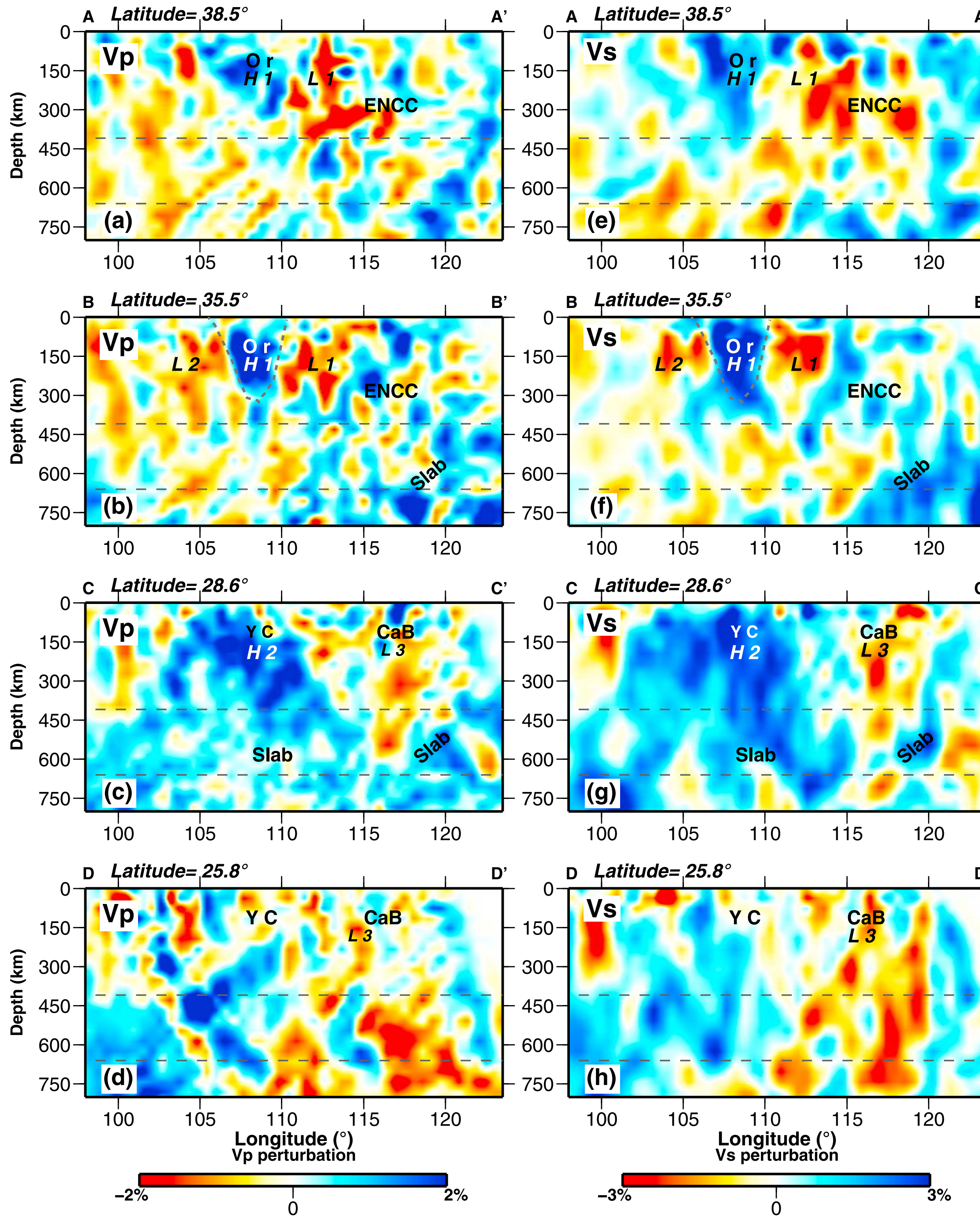

Figure 5. Cross-sections from the V_P and V_S velocity models. The A-A′, B-B′, C-C′ and D-D′ transects are used to present cross-sectional depth slices (Figure 4). Labels refer to regions shown in Figure 1 (e.g., Or, ENCC, YC, CaB). Tags L1–3 and H1–2 represent velocity anomalies described in sections 4 and 5 of the text.

attenuated mantle transition zone beneath the NCC [*Zhu and Zheng*, 2009; *Xu et al.*, 2011].

[22] A high velocity anomaly appears at depths of 430 km and 580 km, immediately east of the area beneath the Tanlu Fault Zone (TLF in Figure 4). We interpret this anomaly as the stagnant slab front of the subducted Pacific Plate [*Huang and Zhao*, 2006; *Li and van der Hilst*, 2010].

4.2. The South China Block

[23] In the SCB, the YC is distinguished from surrounding areas by a laterally continuous upper

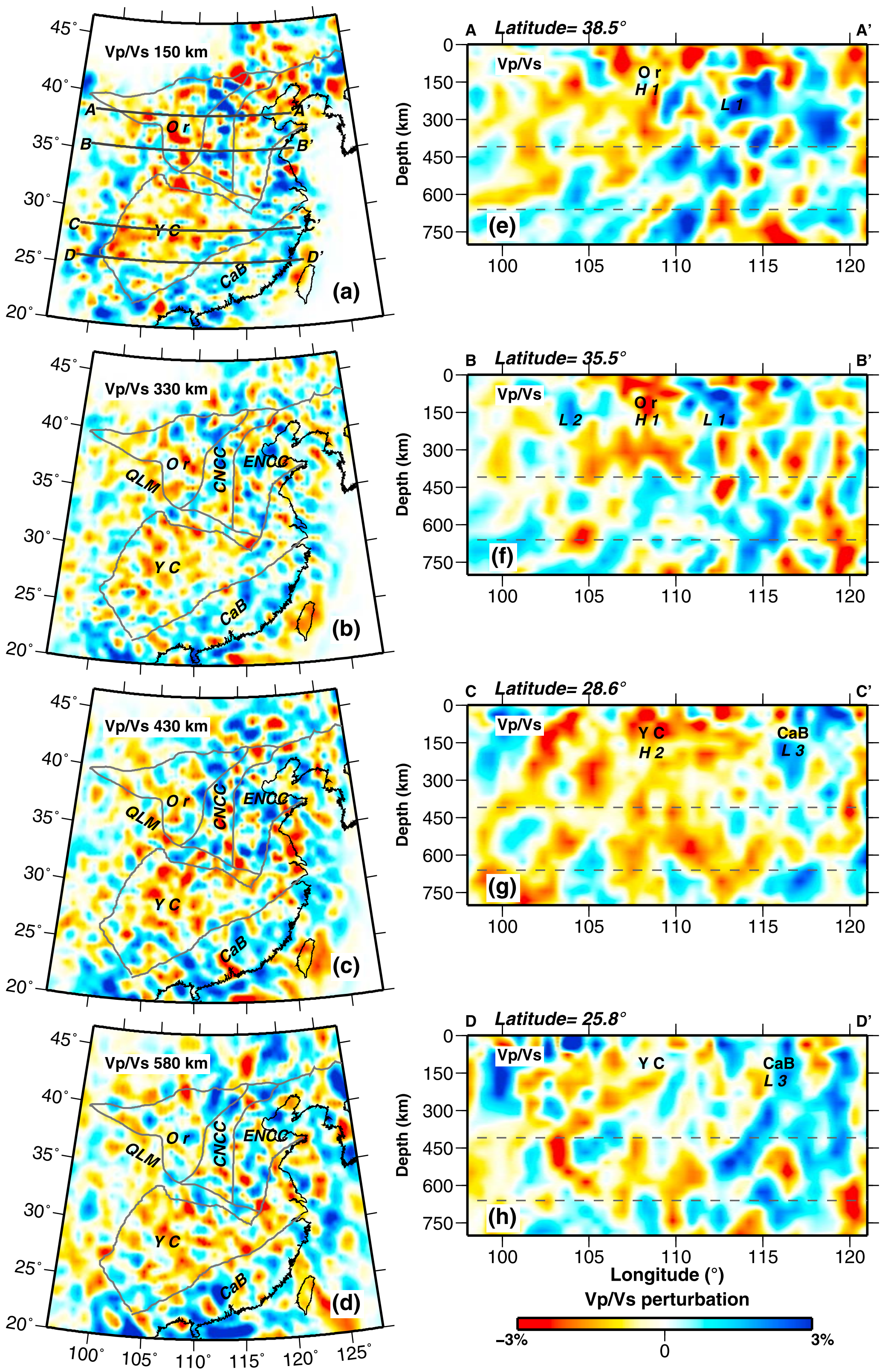

Figure 6. Depth slices and cross-sections from the V_P/V_S velocity models. Tags L1–3 and H1–2 represent velocity anomalies described in sections 4 and 5 of the text.

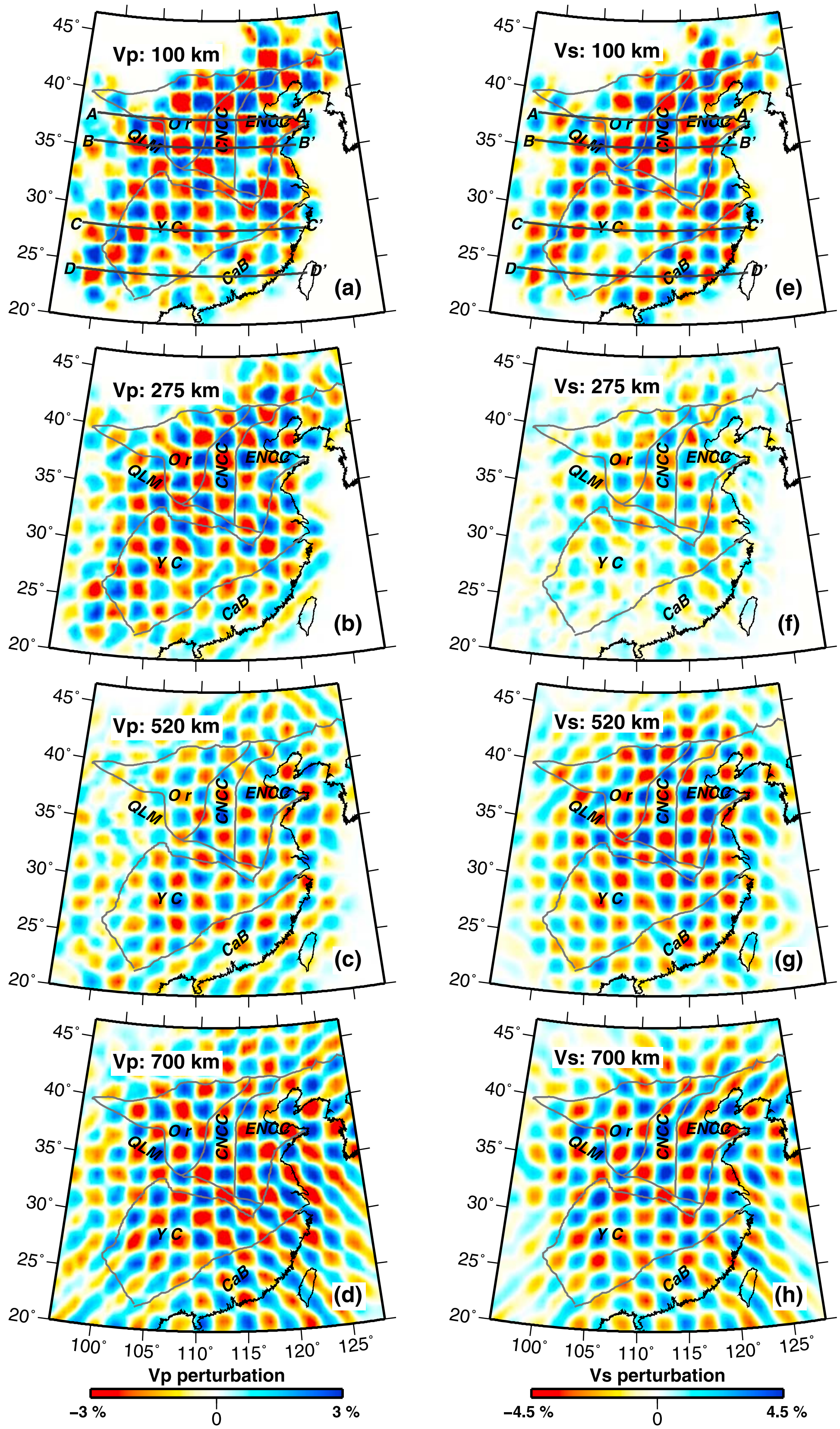

Figure 7. Resolution test results for (a–d) V_P and (e–h) V_S anomalies at different depths.

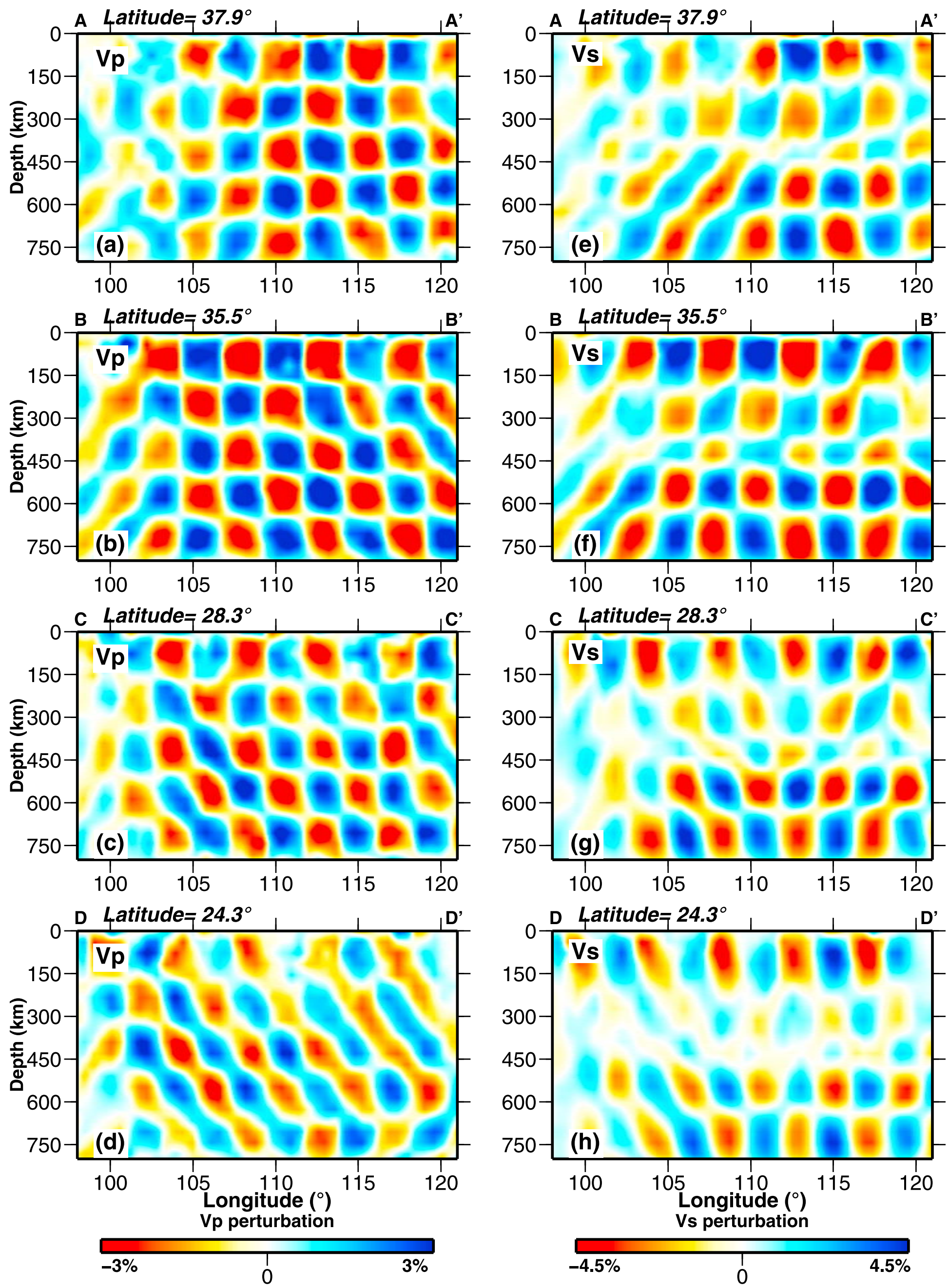

Figure 8. Resolution test results for (a–d) V_P and (e–h) V_S anomalies across transects shown in Figure 5.

mantle anomaly defined by high velocity and low V_P/V_S ratio, and extending from 100 km depth to the mantle transition zone. The largest low-velocity and high V_P/V_S ratio anomalies are found beneath the CaB. This latter anomalous body trends SW-NE and extends from the base of the Cathaysia lithosphere (generally <100 km depth) down to the mantle transition zone. The transitional area between the YC and the CaB roughly coincides with the boundary separating Proterozoic CaB units from older YC units.

5. Resolution Tests

[24] The data set used to construct the tomographic model presented here is sufficient to constrain structures with dimensions of 200 km or more. Multiple resolution tests were used to verify the

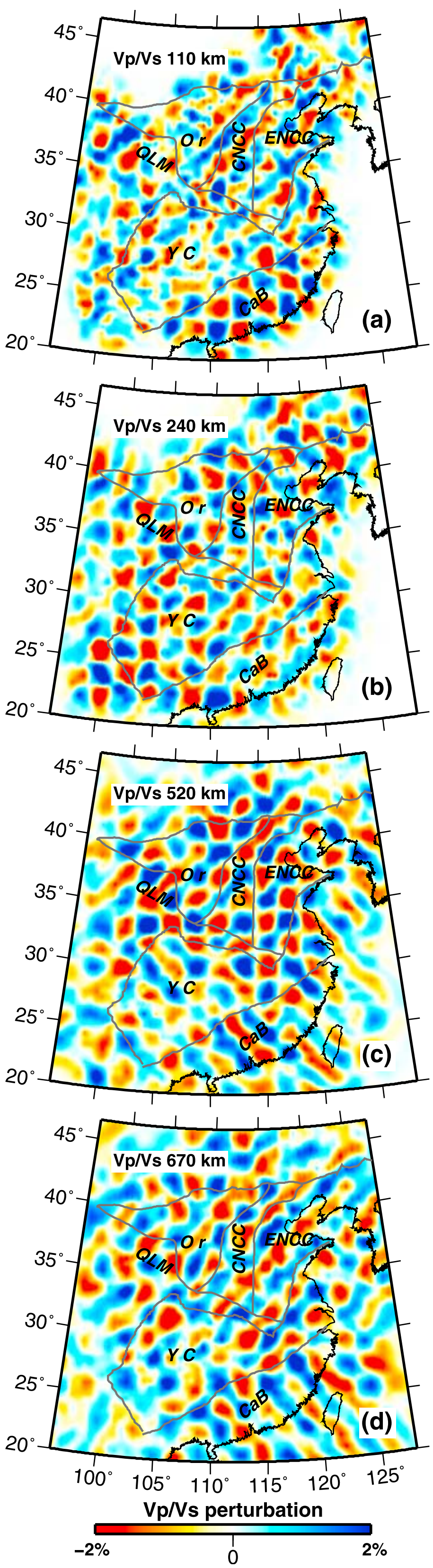

Figure 9. Resolution test results for V_P/V_S ratios at different depths.

robustness of the solution. A synthetic 3-D velocity model generated synthetic travel-time delays for the same paths traversed by the P- and S-waves used to construct the original data set. The velocity model was then inverted to determine if the synthetic velocity structure could be recovered. For each experiment, Gaussian white noise was introduced to the synthetic relative travel-time signals to simulate noise in the data. The artificial noise was scaled to about 15% of the signal, in proportions that exceeded the standard deviation of the travel-time measurements. The same damping parameters were used in the inversions of both the synthetic and empirical data.

[25] We initially conducted checkerboard experiments with alternating high and low velocity anomalies of $\pm3\%$ $\delta\ln V_P$ and $\pm5\%$ $\delta\ln V_S$ within individual blocks measuring 208 km by 208 km in area, by 156 km in depth. The depth slices and cross-sections for V_P and V_S from the recovered models are shown in Figures 7 and 8. The corresponding V_P/V_S ratio anomalies are between $\pm2.1\%$. Depth slices for V_P/V_S ratio are shown in Figure 9. The tests show that the resolution is good down to 700 km depth for anomalies $\geq$200 km, even for data with 15% noise, given adequate regional station coverage. Inspection of the recovered images showed that the location and shape of the structures are clearly rendered. The recovered velocity anomaly amplitudes were slightly reduced.

[26] The second series of tests were performed to test how well the data set resolved vertical and dipping velocity anomalies. Several high- or low-velocity anomalies of varying diameter were assigned to different depth ranges (Figures 10 and 11). Velocity perturbations of $\pm2\%$ $\delta\ln V_P$ and $\pm3\%$ $\delta\ln V_S$ were introduced to each anomaly. Inspection of the recovered images showed that the location and shape of individual anomaly structures were clearly rendered and the vertical smearing length is negligible. The vertical smearing effect was obvious however for a model with a 400 km-wide high-velocity anomaly volume (Figures 10d and 10h; labeled as H2) in the upper mantle located above a high-velocity anomaly (H3 in Figure 10) in the mantle transition zone. We interpret the high-velocity anomaly extending from the base of the lithosphere to the mantle transition zone (H2 in Figures 5c and 5g) beneath the YC as a possible smearing effect. Adjusting the dimension of H3, we also tested the influence of the minimum depth of the H2 anomaly on vertical smearing. The vertical smearing effect is weakened if the base of H2 is shallower than 200 km. This implies that high-velocity anomalies may

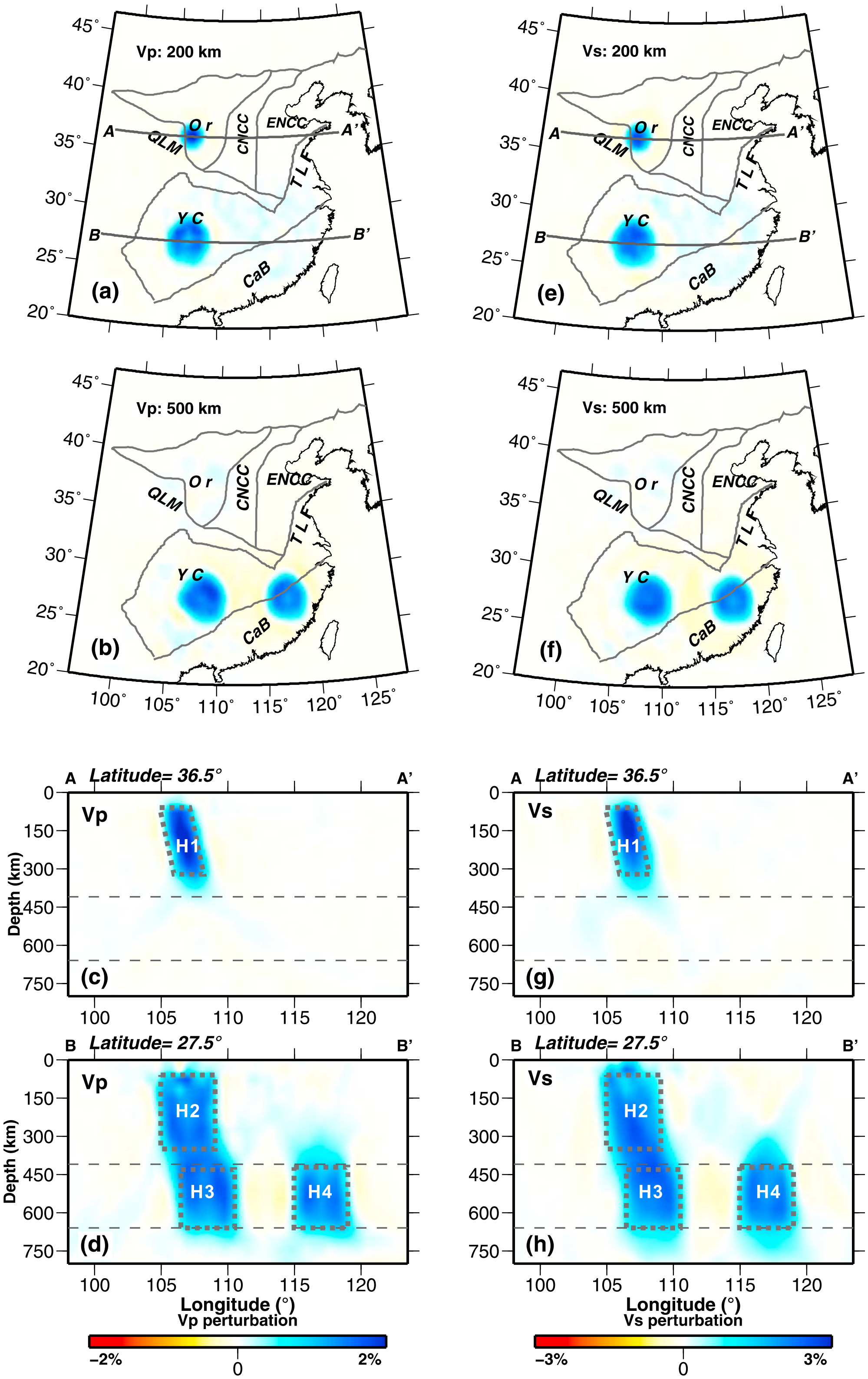

Figure 10. Resolution test results for models with vertical or dipping high-velocity anomalies. Depth slices (at 200 km and 500 km depth) and cross-sections are shown for (a–d) V_P models and (e–h) V_S models. Lines A-A′, B-B′ in upper panels give the locations of cross-sections. Dashed lines define the geometries of the input anomalous volumes.

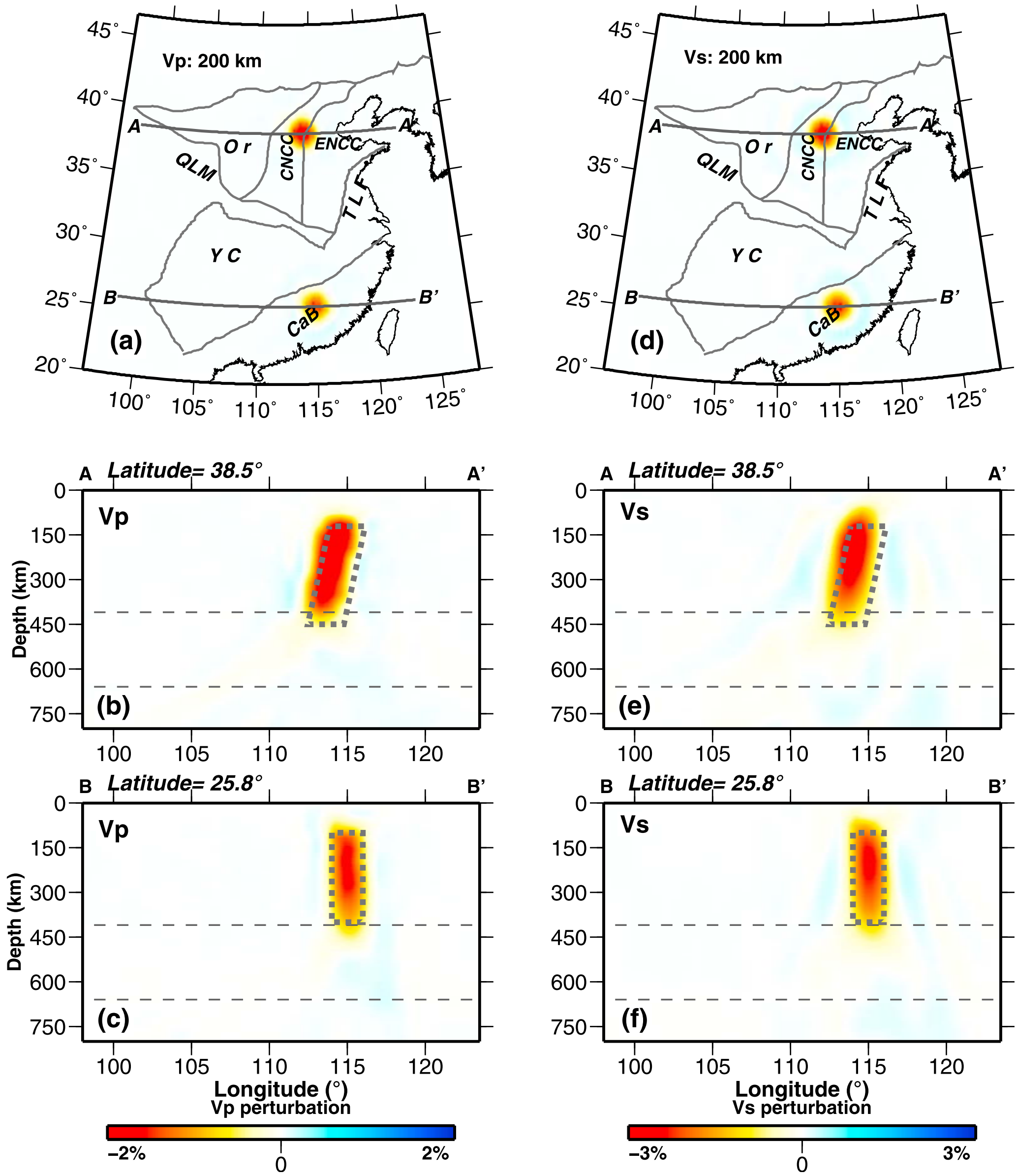

Figure 11. Resolution test results for models with vertical or dipping low-velocity anomalies. Labels are the same as those given in the caption to Figure 10.

coexist both in the upper mantle and the mantle transition zone beneath the YC.

6. Discussions

[27] Seismic heterogeneities inferred from the tomographic models constructed here are strongly correlated with the major tectonic and magmatic features of EC as well as regional geodynamic events. This section discusses the salient features of the V_P, V_S and V_P/V_S models, and enlists tectonic and magmatic evidence to develop unique geodynamic interpretations for different areas of EC.

6.1. Physical Causes of the Velocity Anomalies

[28] Interpretations of velocity anomalies assume that spherically symmetric seismic models of the mantle reflect typical olivine phase transitions in an adiabatic P-T regime [*Cammarano et al.*, 2003]. Mantle material can deviate from this conventional structure due to a combination of physical factors, including temperature anomalies, partial melting, bulk and volatile

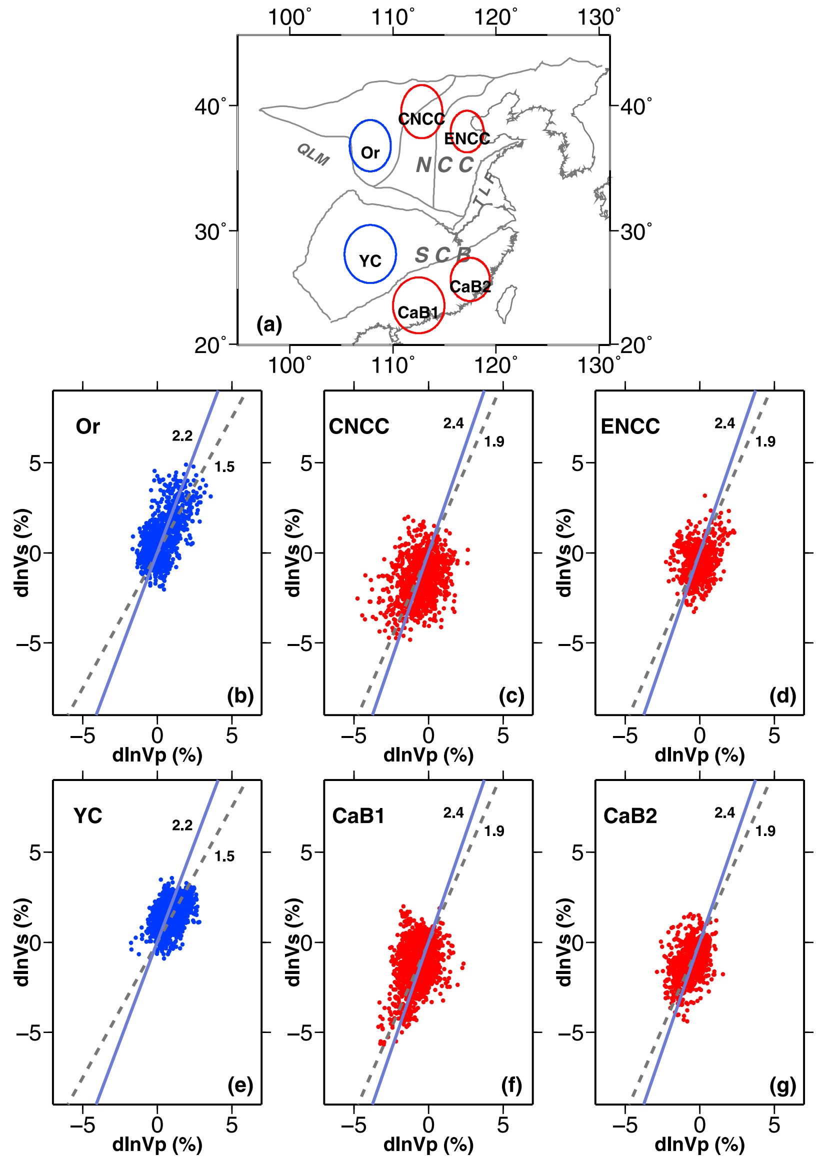

Figure 12. Upper mantle $\partial\ln V_S/\partial\ln V_P$ (depth ranging from 140 km to 660 km) for 6 EC regions. (a) Simple map showing the locations of regions. Blue circles represent cratonic blocks and red circles represent young magmatic provinces. Regions include (b) Ordos Craton, (c) central NCC, (d) eastern NCC (e) YC, and (f and g) areas of the CaB. The dashed black lines and blue lines indicate reference trends with their slope values labeled at top.

compositional heterogeneities, and other forms of anisotropy [*Schmandt and Humphreys*, 2010]. Theoretical models have shown that in the upper mantle, the scale of velocity anomalies reported by recent tomographic studies [e.g., *Schmandt and Humphreys*, 2010] can be primarily attributed to temperature effects and partial melting [*Hammond and Humphreys*, 2000; *Cammarano et al.*, 2003]. It is predicted that a P wave velocity anomaly of $\pm1\%$ corresponds to a temperature perturbation exceeding 100–200 K under dry conditions. The relative sensitivity of S- and P wave velocities to variation in mantle material is apparent as deviation in the V_P/V_S ratio (relative to average values). Calculation of $\partial\ln V_S/\partial\ln V_P$ gave expected values for thermal variations in the upper mantle ranging from 1.3 to 2.2 at low and high temperatures, respectively [*Cammarano et al.*, 2003]. Partial melting in the upper mantle is predicted to attenuate velocities and cause higher $\partial\ln V_S/\partial\ln V_P$ values of $\sim$2.2 to 2.3 [*Hammond and Humphreys*, 2000; *Schmandt and Humphreys*, 2010].

[29] High V_P and V_S volumes, along with low V_P/V_S volumes (H1, H2 in Figure 5) are apparent down to depths of >300 km beneath the Precambrian Ordos block and YC. Figures 12b and 12e show an average

$\partial \ln V_S / \partial \ln V_P$ value of $\sim$1.5 beneath these regions. These observations indicate a subsurface structure having thick lithospheric roots, lower temperatures, and a relatively depleted geochemical composition. The mantle transition zone beneath the YC exhibits high V_P, V_S and low V_P/V_S volumes (Figures 4c, 4d, 4g, 4h, 5c, 5d, 5g, and 5h). This subsurface area also becomes narrower from north to south. We interpret these features as evidence of the stagnant slab of the Paleo-Pacific Plate subducted beneath Southeast China during the Mesozoic [e.g., *Li and van der Hilst*, 2010].

[30] The central and eastern NCC and CaB exhibit low V_P and V_S volumes, and high V_P/V_S volumes (Figures 4 and 6), which are typical of young igneous provinces. The large low-velocity anomaly observed in this region indicates warm mantle material associated with large-scale Mesozoic to Cenozoic igneous features. A majority of the Cenozoic rift systems and basalt deposits in the NCC, including the Shanxi-Shanxi Rift System and the Hannuoba volcanics [*Zhao et al.*, 2009] are located above the low-velocity zones imaged here. The horizontal outline of the low-velocity zone beneath the SCB also coincides with an extensive igneous province [e.g., *Li and Li*, 2007]. Figures 12c and 12d and Figures 12f and 12g show that $\partial \ln V_S / \partial \ln V_P$ values are >2.2 for these magmatic provinces, indicating that partial melting contributes to velocity anomalies beneath these regions.

[31] In general, we interpret the observed V_P, V_S and V_P/V_S variation as evidence of laterally varying temperature differences due to variable lithospheric thickness, asthenospheric features and stagnant slab volumes in the mantle transition zone. Areas having extremely low V_P and V_S anomalies and high V_P/V_S ratio anomalies reflect partial melting beneath EC [e.g., *Goes and van der Lee*, 2002; *Schmandt and Humphreys*, 2010].

6.2. Potential Causes for Spatial Variations in EC Evolution

[32] Geological, geophysical and geochemical evidence suggest that the geodynamic evolution of EC is primarily a controlled by Mesozoic to Cenozoic subduction of the Paleo-Pacific plate [*Wu et al.*, 2005; *Wang et al.*, 2006; *Huang and Zhao*, 2006; *Li and Li*, 2007; *Sun et al.*, 2007; *Zhao et al.*, 2007; *Lin et al.*, 2008]. Differences in the scale of anomalous volumes imaged beneath eastern NCC and the SCB imply distinct geodynamic processes for these regions. Subduction structures and processes appear to be laterally continuous beneath the CaB, but fragmented beneath the eastern NCC. For a given subduction zone, spatial variation in the continental plate's evolution depends on the water content and geometry of the subducting plate, as well as the intrinsic properties of the continental block. Figure 13 presents a hypothetical series of events that explain the causes for spatial variability in EC's response to different stages of subduction.

[33] Differing geometries of the fragmented subducting plate may cause spatial variations in EC evolution and lateral variation in the water-content of the subducting slab would then strengthen these heterogeneities. While the lithospheric thickness of the CaB prior to the Mesozoic is unknown, the NCC and the YC persisted as stable cratons with thick lithospheric roots until the early Paleozoic [e.g., *Menzies et al.*, 1993; *Griffin et al.*, 1998]. With the subduction of the Pacific Plate and eastward retreat of the slab [e.g., *Li and van der Hilst*, 2010], subduction-induced mantle convection beneath EC would induce a temperature increase and partial melting of the uppermost mantle, resulting in the reactivation of EC lithosphere. Previous tomographic models [e.g., *Huang and Zhao*, 2006; *Li and van der Hilst*, 2010] and regional receiver-function images of the mantle transition zone [e.g., *Ai and Zheng*, 2003; *Zhu and Zheng*, 2009; *Chen and Ai*, 2009; *Xu et al.*, 2011] indicate that the slab front of the Pacific Plate extends well into the area beneath the SCB ($\sim$105°E), but only reaches the eastern boundary of the NCC ($\sim$118°E). The impinging slab front would therefore introduce stronger subcrustal material (the slab itself) and enhance convergent flow and thermal convection beneath the SCB, but not beneath the eastern NCC. The offset in the slab front between SCB and NCC explains the larger, laterally continuous low velocity and V_S/V_P ratio anomalies observed in the CaB upper mantle, but not beneath the NCC. The Basin and Range-style rift systems of the SCB and the wide, uninterrupted basins of the NCC indicate that a heterogeneous compressional stress-field affects the former area, but not the latter.

[34] The outlines of velocity anomalies are spatially consistent with major tectonic units and boundaries in the SCB and the CaB. The correspondence of geophysical and geological features suggests the intrinsic properties of both the NCC and SCB also influence mantle-flow patterns. The NCC includes a thick Archean lithospheric component that was attenuated and rifted from Mesozoic to Cenozoic time [e.g., *Griffin et al.*, 1998; *Chen et al.*, 2008; *Zheng et al.*, 2008; *Zhu and Zheng*, 2009]. U-Pb zircon geochronology dates the CaB as Neoproterozoic in age, indicating that it is younger than the

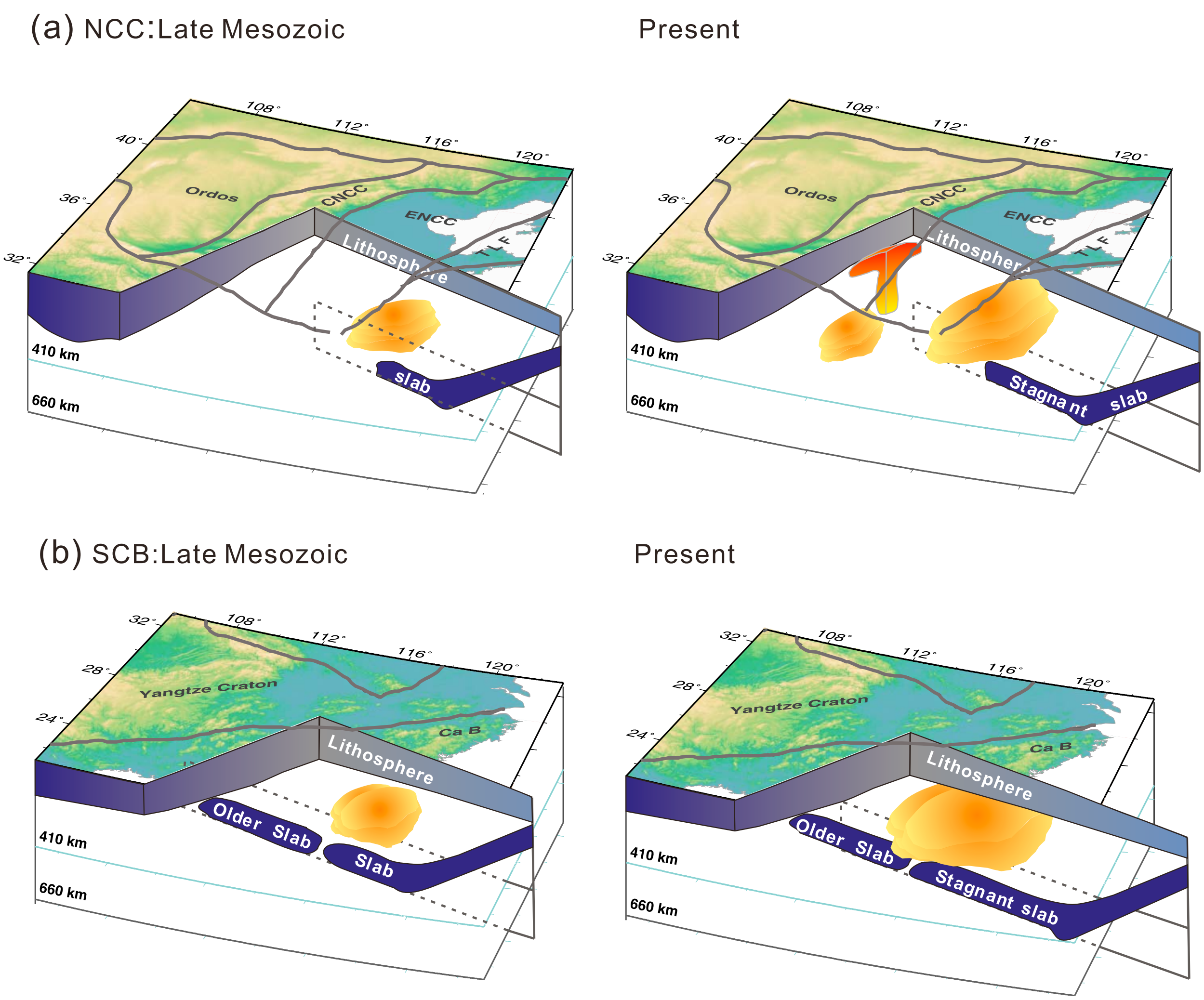

Figure 13. Event history cartoon depicting evolution of EC's upper mantle caused by the Pacific Plate subduction (see texts for details). Grey lines on the surface mark the boundaries of tectonic units; orange areas highlight the low velocity anomalous volumes imaged by our study. The 410 km and 660 km discontinuities of the mantle transition zone are shown on the left. (a) For the NCC the mushroom-like low velocity anomaly represents a possible zone of mantle upwelling beneath the central NCC [*Zhao et al.*, 2009]. (b) For the SCB the slab front has reached ∼105°E as described in this study and previous studies [e.g., *Li et al.*, 2008].

NCC [*Yu et al.*, 2006]. Recent geodynamic models demonstrate that high viscosity conditions or a cold thermal state in the mantle may create localized weak zones when a craton is subjected to extensional stress [*Lu et al.*, 2011]. Given these theoretical constraints, subduction of the Pacific Plate would generate smaller-scale anomalies beneath the older NCC, but produce larger, laterally continuous anomalies beneath the younger CaB.

7. Conclusions

[35] We present new 3-D tomographic models of V_P, V_S and V_P/V_S ratio anomalies that demonstrate strong, multiscale heterogeneities in the upper mantle beneath EC. Resolution tests for different depths and the prominent velocity anomalies identified by our model verify that the tomographic images can resolve velocity heterogeneities in the upper mantle to depths of 700 km.

[36] The anomalous volumes observed beneath the NCC and SCC exhibit a pronounced contrast in scale. These features demonstrate that different areas of EC have differing histories associated with Pacific Plate subduction. Seismic heterogeneities evident from tomographic models are found beneath major tectonic and magmatic features of EC, providing a link between major surface features and

larger-scale geodynamic events. In general, we suggest that most of the observed V_P, V_S and V_P/V_S ratio anomalies reflect variations in lithospheric thickness, asthenospheric conditions, stagnant slab volumes and the associated temperature perturbations. The strongest observed anomalies are likely due to areas of partial melting beneath EC.

[37] We attribute the spatial variation in EC's response to ongoing subduction related deformation to two mechanisms. First, the subducting slab reaches further beneath the SCB in the westward direction and thus subjected this region to greater tectonic stress, introduced more subduction related material and strengthened thermal convection. The slab does not significantly impinge past the eastern boundary of the NCC, resulting in fewer observed anomalies. Second, the eastern NCC consists of an older Archean lithospheric component having a colder thermal state, stronger rheology and smaller-scale heterogeneities. In contrast, the younger Neoproterozoic CaB has a warmer thermal state and weaker rheology. This latter region therefore exhibits more continuous deformational features relative to the NCC.

Acknowledgments

[38] We thank Xiufen Zheng, Mingming Jiang, Yinshuang Ai and Ling Chen for their help with data collection. Discussions with Mathias Obrebski, Ling Chen, Wei Lin, and Gang Lu improved the manuscript. We thank Editor Thorsten Becker, the associate editor, Yang Shen and an anonymous reviewer for very helpful reviews. Waveform data are provided by Seismological Laboratory, IGGCAS and Data Management Centre of China National Seismic Network at Institute of Geophysics, China Earthquake Administration. This research was financially supported by Chinese Academy of Sciences (grant KZCX2-YW-QN102), the NSFC grant 90914011 and 40974030.

References

Ai, Y., and T. Zheng (2003), The upper mantle discontinuity structure beneath eastern China, *Geophys. Res. Lett.*, *30*(21), 2089, doi:10.1029/2003GL017678.

Ai, Y., Q. Chen, F. Zeng, X. Hong, and W. Ye (2007), The crust and upper mantle structure beneath southeastern China, *Earth Planet. Sci. Lett.*, *260*, 549–563, doi:10.1016/j.epsl.2007.06.009.

Allen, R. M., et al. (2002), Imaging the mantle beneath Iceland using integrated seismological techniques, *J. Geophys. Res.*, *107*(B12), 2325, doi:10.1029/2001JB000595.

Cammarano, F., S. Goes, P. Vacher, and D. Giardini (2003), Inferring upper-mantle temperatures from seismic velocity, *Phys. Earth Planet. Inter.*, *138*, 197–222, doi:10.1016/S0031-9201(03)00156-0.

Chang, X., K. Liu, J. He, and H. Sun (2007), Lower velocities beneath the Taihang Mountains, Northeastern China, *Bull. Seismol. Soc. Am.*, *97*, 1364–1369, doi:10.1785/0120060210.

Chen, L., and Y. Ai (2009), Discontinuity structure of the mantle transition zone beneath the North China Craton from receiver function migration, *J. Geophys. Res.*, *114*, B06307, doi:10.1029/2008JB006221.

Chen, L., T. Wang, L. Zhao, and T. Zheng (2008), Distinct lateral variation of lithospheric thickness in the Northeastern North China Craton, *Earth Planet. Sci. Lett.*, *267*, 56–68, doi:10.1016/j.epsl.2007.11.024.

Dahlen, F. A., S. H. Hung, and G. Nolet (2000), Fréchet kernels for finite-frequency traveltimes–I. Theory, *Geophys. J. Int.*, *141*, 157–174, doi:10.1046/j.1365-246X.2000.00070.x.

Ekström, G., and A. M. Dziewonski (1998), The unique anisotropy of the Pacific upper mantle, *Nature*, *394*, 168–172, doi:10.1038/28148.

Faure, M., W. Lin, and N. L. Breton (2001), Where is the North China–South China block boundary in eastern China?, *Geology*, *29*, 119–122, doi:10.1130/0091-7613(2001)029<0119:WITNCS>2.0.CO;2.

Feng, M., S. van der Lee, M. An, and Y. Zhao (2010), Lithospheric thickness, thinning, subduction, and interaction with the asthenosphere beneath China from the joint inversion of seismic S-wave train fits and Rayleigh-wave dispersion curves, *Lithos*, *120*, 116–130, doi:10.1016/j.lithos.2009.11.017.

Goes, S., and S. van der Lee (2002), Thermal structure of the North American uppermost mantle inferred from seismic tomography, *J. Geophys. Res.*, *107*(B3), 2050, doi:10.1029/2000JB000049.

Griffin, W. L., A. D. Zhang, S. Y. O'Reilly, and C. G. Ryan (1998), Phanerozoic evolution of the lithosphere beneath the Sino-Korean craton, in *Mantle Dynamics and Plate Interactions in East Asia*, *Geodyn. Ser.*, vol. 27, edited by M. F. J. Flower et al., pp. 107–126, AGU, Washington, D. C., doi:10.1029/GD027p0107.

Gripp, A. E., and R. G. Gordon (2002), Young tracks of hotspots and current plate velocities, *Geophys. J. Int.*, *150*, 321–361, doi:10.1046/j.1365-246X.2002.01627.x.

Hammond, W. C., and E. D. Humphreys (2000), Upper mantle seismic wave velocity: Effects of realistic partial melt geometries, *J. Geophys. Res.*, *105*, 10,975–10,986, doi:10.1029/2000JB900041.

Hearn, T. M., S. Wang, J. F. Ni, Z. Xu, Y. Yu, and X. Zhang (2004), Uppermost mantle velocities beneath China and surrounding regions, *J. Geophys. Res.*, *109*, B11301, doi:10.1029/2003JB002874.

Hu, S., L. He, and J. Wang (2000), Heat flow in the continental area of China: A new data set, *Earth Planet. Sci. Lett.*, *179*, 407–419, doi:10.1016/S0012-821X(00)00126-6.

Huang, J., and D. Zhao (2006), High-resolution mantle tomography of China and surrounding regions, *J. Geophys. Res.*, *111*, B09305, doi:10.1029/2005JB004066.

Huang, Z., W. Su, Y. Peng, Y. Zheng, and H. Li (2003), Rayleigh wave tomography of China and adjacent regions, *J. Geophys. Res.*, *108*(B2), 2073, doi:10.1029/2001JB001696.

Huang Z., H. Li, Y. Zheng, and Y. Peng (2009), The lithosphere of North China Craton from surface wave tomography, *Earth Planet. Sci. Lett.*, *288*, 164–173, doi:10.1016/j.epsl.2009.09.019.

Hung, S., F. A. Dahlen, and G. Nolet (2000), Fréchet kennels for finite-frequency traveltimes-II, Examples, *Geophys. J. Int.*, *141*, 175–203, doi:10.1046/j.1365-246X.2000.00072.x.

Hung, S., Y. Shen, and L. Chiao (2004), Imaging seismic velocity structure beneath the Iceland hot spot: A finite frequency approach, *J. Geophys. Res.*, *109*, B08305, doi:10.1029/2003JB002889.

Jiao, W. F., Y. B. Wu, S. H. Yang, M. Peng, and J. Wang (2009), The oldest basement rock in the Yangtze Craton revealed by zircon U-Pb age and Hf isotope composition, *Sci. Chin. Ser. D Earth Sci.*, *52*, 1393–1399, doi:10.1007/s11430-009-0135-7.

Kennett, B. L. N., and E. R. Engdahl (1991), Traveltimes for global earthquake location and phase identification, *Geophys. J. Int.*, *105*, 429–465, doi:10.1111/j.1365-246X.1991.tb06724.x.

Koulakov, I., M. K. Kaban, M. Tesauro, and S. Cloetingh (2009), P- and S-velocity anomalies in the upper mantle beneath Europe from tomographic inversion of ISC data, *Geophys. J. Int.*, *179*, 345–366, doi:10.1111/j.1365-246X.2009.04279.x.

Lebedev, S., and G. Nolet (2003), Upper mantle beneath Southeast Asia from S velocity tomography, *J. Geophys. Res.*, *108*(B1), 2048, doi:10.1029/2000JB000073.

Lei, J., and D. Zhao (2005), P wave tomography and origin of the Changbai intraplate volcano in northeast Asia, *Tectonophysics*, *397*, 281–295, doi:10.1016/j.tecto.2004.12.009.

Li, C., and R. D. van der Hilst (2010), Structure of the upper mantle and transition zone beneath Southeast Asia from traveltime tomography, *J. Geophys. Res.*, *115*, B07308, doi:10.1029/2009JB006882.

Li, C., R. D. van der Hilst, and M. N. Toksöz (2006), Constraining P wave velocity variations in the upper mantle beneath Southeast Asia, *Phys. Earth Planet. Inter.*, *154*, 180–195, doi:10.1016/j.pepi.2005.09.008.

Li, C., R. D. van der Hilst, E. R. Engdahl, and S. Burdick (2008), A new global model for P wave speed variations in Earth's mantle, *Geochem. Geophys. Geosyst.*, *9*, Q05018, doi:10.1029/2007GC001806.

Li, X. H. (2000), Cretaceous magmatism and lithospheric extension in Southeast China, *J. Southeast Asian Sci.*, *18*, 293–305.

Li, X. H., Z. X. Li, B. He, W. X. Li, Q. L. Li, Y. Y. Gao, and X. C. Wang (2012), The Early Permian active continental margin and crustal growth of the Cathaysia Block: *In situ* U–Pb, Lu–Hf and O isotope analyses of detrital zircons, *Chem. Geol.*, doi:10.1016/j.chemgeo.2011.10.027, in press.

Li, Z. X., and X. H. Li (2007), Formation of the 1300 km-wide intra-continental orogen and post-orogenic magmatic province in Mesozoic South China: A flat-slab subduction model, *Geology*, *35*, 179–182, doi:10.1130/G23193A.1.

Lin, W., Q. Wang, and K. Chen (2008), Phanerozoic tectonics of south China block: New insights from the polyphase deformation in the Yunkai massif, *Tectonics*, *27*, TC6004, doi:10.1029/2007TC002207.

Liu, C. Z., Z. C. Liu, F. Y. Wu, and Z. Y. Chu (2012), Mesozoic accretion of juvenile sub-continental lithospheric mantle beneath South China and its implications: Geochemical and Re–Os isotopic results from Ningyuan mantle xenoliths, *Chem. Geol.*, *291*, 186–198, doi:10.1016/j.chemgeo.2011.10.006.

Liu, D. Y., A. P. Nutman, W. Compston, J. S. Wu, and Q. H. Shen (1992), Remnants of 3800 Ma crust in the Chinese part of the Sino-Korean craton, *Geology*, *20*, 339–342, doi:10.1130/0091-7613(1992)020<0339:ROMCIT>2.3.CO;2.

Lu, G., B. Kaus, and L. Zhao (2011), Thermal localization as a potential mechanism for craton breakup, *Phys. Earth. Planet. Inter.*, *186*, 125–137, doi:10.1016/j.pepi.2011.04.006.

Meng, Q. R., and G. W. Zhang (2000), Geologic framework and tectonic evolution of the Qinling orogen, central China, *Tectonophysics*, *323*, 183–196, doi:10.1016/S0040-1951(00)00106-2.

Meng, Q. R., E. Wang, and J. M. Hu (2005), Mesozoic sedimentary evolution of the northwest Sichuan basin: Implication for continued clockwise rotation of the South China block, *Geol. Soc. Am. Bull.*, *117*, 396–410, doi:10.1130/B25407.1.

Menzies, M. A., W. M. Fan, and M. Zhang (1993), Palaeozoic and Cenozoic lithoprobes and the loss of >120 km of Archean lithosphere, Sino-Korean craton, China, in *Magmatic Processes and Plate Tectonics*, edited by H. M. Prichard et al., *Geol. Soc Spec. Publ.*, *76*, 71–81, doi:10.1144/GSL.SP.1993.076.01.04.

Niu, Y. L. (2005), Generation and evolution of basaltic magmas: Some basic concepts and a new view on the origin of Mesozoic-Cenozoic basaltic volcanism in eastern China, *Geol. J. Chin. Univ.*, *11*, 9–46.

Obrebski, M., R. M. Allen, F. Zhang, J. Pan, Q. Wu, and S.-H. Hung (2012), Shear wave tomography of China using joint inversion of body and surface wave constraints, *J. Geophys. Res.*, *117*, B01311, doi:10.1029/2011JB008349.

Paige, C. C., and M. A. Saunders (1982), LSQR: An algorithm for sparse linear-equations and sparse least-squares, *Trans. Math. Software*, *8*, 43–71, doi:10.1145/355984.355989.

Ren, J., K. Tamaki, S. Li, and J. X. Zhang (2002), Late Mesozoic and Cenozoic rifting and its dynamic setting in Eastern China and adjacent areas, *Tectonophysics*, *344*, 175–205, doi:10.1016/S0040-1951(01)00271-2.

Schmandt, B., and E. Humphreys (2010), Complex subduction and small-scale convection revealed by body-wave tomography of the western United States upper mantle, *Earth Planet. Sci. Lett.*, *297*, 435–445, doi:10.1016/j.epsl.2010.06.047.

Sun, W. D., X. Ding, Y. H. Hu, and X. H. Li (2007), The golden transformation of the Cretaceous plate subduction in the west Pacific, *Earth Planet. Sci. Lett.*, *262*, 533–542, doi:10.1016/j.epsl.2007.08.021.

Sun, Y., and M. N. Toksöz (2006), Crustal structure of China and surrounding regions from P wave traveltime tomography, *J. Geophys. Res.*, *111*, B03310, doi:10.1029/2005JB003962.

Sun, Y., M. N. Toksöz, S. Pei, D. Zhao, F. D. Morgan, and A. Rosca (2008a), S wave tomography of the crust and uppermost mantle in China, *J. Geophys. Res.*, *113*, B11307, doi:10.1029/2008JB005836.

Sun, Y., M. N. Toksöz, S. Pei, and F. D. Morgan (2008b), The layered shear wave velocity structure of the crust and uppermost mantle in China, *Bull. Seismol. Soc. Am.*, *98*, 746–755, doi:10.1785/0120050222.

Tian, Y., D. Zhao, R. Sun, and J. Teng (2009), Seismic imaging of the crust and upper mantle beneath the North China craton, *Phys. Earth. Planet. Inter.*, *172*, 169–182, doi:10.1016/j.pepi.2008.09.002.

Vandecar, J. C., and R. S. Crosson (1990), Determination of teleseismic relative phase arrival Times using multi-channel cross-correlation and least-squares, *Bull. Seismol. Soc. Am.*, *80*, 150–169.

Wang, F., X. H. Zhou, L. C. Zhang, J. F. Ying, Y. T. Zhang, F. Y. Wu, and R. X. Zhu (2006), Late Mesozoic volcanism in the Great Xing'an Range (NE) China: Timing and implications for the dynamic setting of NE Asia, *Earth Planet. Sci. Lett.*, *251*, 179–198, doi:10.1016/j.epsl.2006.09.007.

Wang, Q., J. W. Li, P. Jian, Z. H. Zhao, X. L. Xiong, Z. W. Bao, J. F. Xu, C. F. Li, and J. L. Ma (2005), Alkaline syenites in eastern Cathaysia (South China): Link to Permian-Triassic transtension, *Earth Planet. Sci. Lett.*, *230*, 339–354, doi:10.1016/j.epsl.2004.11.023.

Wei, Z. G., L. Chen, and W. Xu (2011), Crustal thickness and Vp/Vs ratio of the central and western North China Craton and its tectonic implications, *Geophys. J. Int.*, *186*, 385–389, doi:10.1111/j.1365-246X.2011.05089.x.

Wen, L., and D. L. Anderson (1995), the fate of the slabs inferred from seismic tomography and 130 Ma subduction, *Earth Planet. Sci. Lett.*, *133*, 185–198, doi:10.1016/0012-821X(95)00064-J.

Wu, F. Y., R. J. Walker, X. W. Ren, D. Y. Sun, and X. H. Zhou (2003), Osmium isotopic constraints on the age of lithospheric mantle beneath northeastern China, *Chem. Geol.*, *196*, 107–129, doi:10.1016/S0009-2541(02)00409-6.

Wu, F. Y., J. Q. Lin, S. A. Wilde, X. O. Zhang, and J. H. Yang (2005), Nature and significance of the Early Cretaceous giant igneous event in eastern China, *Earth Planet. Sci. Lett.*, *233*, 103–119, doi:10.1016/j.epsl.2005.02.019.

Wu, F. Y., D. Sun, W. Ge, Y. Zhang, M. L. Grant, S. A. Wilde, and B. M. Jahn (2011), Geochronology of the Phanerozoic granitoids in northeastern China, *J. Asian Earth Sci.*, *41*, 1–30, doi:10.1016/j.jseaes.2010.11.014.

Xiang, H., L. Zhang, H. W. Zhou, Z. Q. Zhong, W. Zeng, R. Liu, and S. Jin (2008), U-Pb zircon geochronology and Hf isotope study of metamorphosed basic-ultrabasic rocks from metamorphic basement in southwestern Zhejiang: The response of the Cathaysia Block to Indosinian orogenic event, *Sci. China, Ser. D Earth Sci.*, *51*, 788–800, doi:10.1007/s11430-008-0053-0.

Xiao, W. J., B. F. Windley, J. Hao, and M. G. Zhai (2003), Accretion leading to collision and the Permian Solonker suture, Inner Mongolia, China: Termination of the Central Asian orogenic belt, *Tectonics*, *22*(6), 1069, doi:10.1029/2002TC001484.

Xu, P., and D. Zhao (2009), Upper-mantle velocity structure beneath the North China Craton: Implications for lithospheric thinning, *Geophys. J. Int.*, *177*, 1279–1283, doi:10.1111/j.1365-246X.2009.04120.x.

Xu, W. W., T. Y. Zheng, and L. Zhao (2011), Mantle dynamics of the reactivating North China Craton: Constraints from the topographies of the 410-km and 660-km discontinuities, *Sci. Chin. Earth Sci.*, *54*, 881–887, doi:10.1007/s11430-010-4163-0.

Yang, J. H., F. Y. Wu, S. A. Wilde, E. Belousova, and W. L. Griffin (2008), Mesozoic decratonization of the North China block, *Geology*, *36*, 467–470, doi:10.1130/G24518A.1.

Yin, A. (2010), Cenozoic tectonic evolution of Asia: Preliminary synthesis, *Tectonophysics*, *488*, 293–325, doi:10.1016/j.tecto.2009.06.002.

Yu, J., W. Shen, L. Wang, L. Shu, and T. Sun (2006), Cathaysia block: A young continent composed of ancient materials, *Geol. J. Chin. Univ.*, *12*, 440–447.

Zhang, K. (1997), North and South China collision along the eastern and southern North China margins, *Tectonophysics*, *270*, 145–156, doi:10.1016/S0040-1951(96)00208-9.

Zhao, D., J. Lei, and Y. Tang (2004), Origin of the Changbai volcano in northeast China: Evidence from seismic tomography, *Chin. Sci. Bull.*, *49*, 1401–1408, doi:10.1360/04wd0125.

Zhao, D., S. Maruyama, and S. Omori (2007), Mantle dynamics of Western Pacific and East Asia: Insight from seismic tomography and mineral physics, *Gondwana Res.*, *11*, 120–131, doi:10.1016/j.gr.2006.06.006.

Zhao, G. C., S. A. Wilde, P. A. Cawood, and M. Sun (2001), Archean blocks and their boundaries in the North China Craton: Lithological, geochemical, structural and P-T path constraints and tectonic evolution, *Precambrian Res.*, *107*, 45–73, doi:10.1016/S0301-9268(00)00154-6.

Zhao, L., and M. Xue (2010), Mantle flow pattern and geodynamic cause of the North China Craton reactivation: Evidence from seismic anisotropy, *Geochem. Geophys. Geosyst.*, *11*, Q07010, doi:10.1029/2010GC003068.

Zhao, L., R. M. Allen, T. Y. Zheng, and S. Hung (2009), Reactivation of an Archean craton: Constraints from P- and S-wave tomography in North China, *Geophys. Res. Lett.*, *36*, L17306, doi:10.1029/2009GL039781.

Zhao, L., T. Y. Zheng, G. Lu, and Y. S. Ai (2011), No direct correlation of mantle flow beneath the North China Craton to the India-Eurasia collision: Constraints from new SKS wave splitting measurements, *Geophys. J. Int.*, *187*, 1027–1037, doi:10.1111/j.1365-246X.2011.05201.x.

Zhao, X. X., and R. S. Coe (1987), Paleomagnetic constraints on the collision and rotation of north and south China, *Nature*, *327*, 141–144, doi:10.1038/327141a0.

Zheng, T. Y., L. Zhao, W. W. Xu, and R. X. Zhu (2008), Insight into modification of North China Craton from seismological study in the Shandong Province, *Geophys. Res. Lett.*, *35*, L22305, doi:10.1029/2008GL035661.

Zheng, X. F., Z. X. Yao, J. H. Liang, and J. Zheng (2010), The role played and opportunities provided by IGP DMC of China National Seismic Network in Wenchuan, *Bull. Seismol. Soc. Am.*, *100*, 2866–2872, doi:10.1785/0120090257.

Zheng, T. Y., R. X. Zhu, L. Zhao, and Y. S. Ai (2012), Intralithospheric mantle structures recorded continental subduction, *J. Geophys. Res.*, *117*, B03308, doi:10.1029/2011JB008873.

Zhou, X. M., and W. X. Li (2000), Origin of Late Mesozoic igneous rocks in Southeastern China: Implications for lithosphere subduction and underplating of mafic magmas, *Tectonophysics*, *326*, 269–287, doi:10.1016/S0040-1951(00)00120-7.

Zhu, R., and T. Zheng (2009), Destruction geodynamics of the North China craton and its Paleoproterozoic plate tectonics, *Chin. Sci. Bull.*, *54*, 3354–3366, doi:10.1007/s11434-009-0451-5.